Science of Remote Sensing 4 (2021) 100026

Contents lists available at ScienceDirect

Science of Remote Sensing

journal homepage: www.sciencedirect.com/journal/science-of-remote-sensing

Can Landsat 7 preserve its science capability with a drifting orbit?

Shi Qiu [a], Zhe Zhu [a,*], Rong Shang [a], Christopher J. Crawford [b]

[a] Department of Natural Resources and the Environment, University of Connecticut, Storrs, CT, 06269, USA
[b] U.S. Geological Survey (USGS) Earth Resources Observation and Science (EROS) Center, Integrated Science and Applications Branch, 47914 252nd Street, Sioux Falls, SD, 57198, USA

ARTICLE INFO

Keywords:
Landsat 7
EO-1
Orbit drift
BRDF
Time series
Science capability

ABSTRACT

Since 2017, the orbit of Landsat 7 has drifted outside its nominal mission requirement toward an earlier acquisition time because of limited onboard fuel resources. This makes quantitative analyses from Landsat 7 data potentially unreliable for many scientific studies. To comprehensively understand the effect of ongoing (2018–2020) orbit drift on Landsat 7 data, we compared surface reflectance and Top-Of-Atmosphere (TOA) reflectance of growing season observations (July 1 ± 30 days) from Landsat 7 with orbit drift and Landsat 8 with nominal orbit using a total of 10,000 randomly selected Northern Hemisphere (0–75^0 N) terrestrial pixels. To evaluate the future (2021–2023) effect of Landsat 7's orbit drift, we analyzed the historical Northern Hemisphere terrestrial growing season Earth Observing-1 (EO-1) TOA reflectance images, which shared a similar orbit drift as Landsat 7 but occurred much earlier. Results suggest that Landsat 7's orbit drift has already led to a general decrease in surface reflectance and TOA reflectance in 2019 and 2020, with a limited impact (overall reflectance changes less than 0.007). The influence of orbit drift is more substantial for the two shortwave infrared (SWIR) bands and the near infrared (NIR) band, but less for the three visible bands (i.e., Red, Green, and Blue). The Normalized Difference Vegetation Index (NDVI), derived from either surface reflectance or TOA reflectance, increased less than 0.003 in 2020. According to the historical EO-1 TOA reflectance data, we estimate that the effect of Landsat 7's orbit drift will be much more dramatic in the future (e.g., the NIR and SWIR bands will decrease more than 0.015 since July 1, 2021), and for different land cover types, the effects of orbit drift are also quite different. To reduce this influence, we examined the c-factor Bidirectional Reflectance Distribution Function (BRDF) normalization approach to correct the orbit drift impact for Landsat 7 surface reflectance data collected between 2019 and 2020. We found that the c-factor BRDF can reduce the data difference substantially, but how this approach works after Landsat 7's orbit drifts further still requires more investigation. Therefore, we determined that Landsat 7 can preserve its science capability until 2020, but will be less reliable for remote sensing applications that need accurate absolute radiometric values after 2020. Correction methods such as c-factor BRDF could be a potential viable approach to maintain its science capability going forward.

1. Introduction

The Landsat program, jointly managed and operated by the National Aeronautics and Space Administration (NASA) and U.S. Geological Survey (USGS), provides the longest and continuous record of Earth's land surface observations free of charge at medium resolution since 1972 (Woodcock et al., 2008; Wulder et al., 2019; Zhu et al., 2019). So far, a total of seven Landsat satellites has been successfully launched, and currently two of the Landsat satellites (Landsat 7 and 8) are still actively collecting Earth observations. Landsat 7, with the Enhanced Thematic Mapper Plus (ETM+) sensor, was launched on April 15, 1999, and has been operating for more than 20+ years. Even though Landsat 7 data have been hampered by the Scan Line Corrector (SLC) off issue since 2003, with a 22% data loss (Loveland and Dwyer, 2012), the recent development of time series analysis based on all available clear observations has made Landsat 7 of the similar value of other Landsats (Zhu, 2017).

To maintain Landsat 7's normal image acquisition mission requirement, the Flight Operations Team (FOT) has made routine "velocity" and "inclination" maneuvers to maintain the sun-synchronous orbit at 705 km with a mean local acquisition time of 10 a.m. ± 15 min overpass at the equator (Fig. 1). On February 7, 2017, however, due to the limited

* Corresponding author.
E-mail address: zhe@uconn.edu (Z. Zhu).

https://doi.org/10.1016/j.srs.2021.100026
Received 18 April 2021; Received in revised form 22 July 2021; Accepted 17 August 2021
Available online 18 August 2021

Fig. 1. Illustration of velocity and inclination maneuvers for maintaining Landsat 7's orbit. The velocity maneuvers maintain Landsat 7 at an altitude of 705 km, and the inclination maneuvers control the acquisition time. Without inclination maneuvers, Landsat 7's orbit will drift toward the West due to the Earth rotation and result in earlier acquisition time. WRS-2: Worldwide Reference System Two.

fuel resources remaining, the FOT made a final "inclination" maneuver to maintain the acquisition time for the last time. This maneuver resulted in a maximum mean local acquisition time of 10:14:18 a.m. on August 12, 2017, and Landsat 7 has been drifting continuously toward an earlier local acquisition time ever since (red dots in Fig. 2). Although Landsat 7 is still operating at a relatively constant altitude, controlled by "velocity" maneuvers (consuming less fuel than "inclination" maneuvers), the earlier local acquisition time will have impacts on its observations and make quantitative analysis from Landsat 7 potentially unreliable for many scientific applications such as land surface change detection (Brown et al., 2020; DeVries et al., 2015; Kennedy et al., 2010; Zhu and Woodcock, 2014) and vegetation greenness trend analyses (Ju and Masek, 2016; Sulla-Menashe et al., 2018; Zhou et al., 2014; Zhu et al., 2016). Therefore, it is critical to quantitatively assess the impact of Landsat 7's orbit drift on its observations.

Orbit drift affects Landsat 7's observations due to changes in solar angles (particularly zenith angle) caused by the earlier local acquisition time (Fig. 2). This impact could be quantified and modeled by using the scattering Bidirectional Reflectance Distribution Function (BRDF) of a particular reflective target, which is a function of both illumination and view geometry. Since the view geometry of Landsat 7 is relatively stable when its orbit is drifting, the BRDF impact is mostly dominated by changes in the solar illumination angle. Historically, Landsat 5 also experienced orbit changes from 1995 to 2000, and from 2003 to 2007, caused by the irregular station keeping maneuvers. Based on a collection of BRDF measurements, Gao et al. (2014) found that the strongest abnormal change of Landsat 5's orbit occurred in 1996, which could change nadir view reflectance around 0.01–0.02 for Red and NIR bands, particularly over shrubland pixels. Zhang and Roy (2016) and Roy et al. (2020) also examined the effect of Landsat 5's orbit change for data collected within the conterminous United States, based on the RossThick-LiSparse-Reciprocal BRDF model (Li and Strahler, 1992; Ross, 1981; Roujean et al., 1992) and U.S. Landsat Analysis Ready Data (ARD) surface reflectance products (Dwyer et al., 2018). They found that Landsat 5's orbit change has led to a maximum acquisition time difference of about 1 h as well as a solar zenith angle variation of more than 10°. Moreover, they also found that orbit change affected the temporal consistency of Landsat 5 observations, particularly for Red and SWIR surface reflectance and Normalized Difference Vegetation Index (NDVI).

These findings for Landsat 5 are helpful but may not be applicable to Landsat 7, which has and will have a very different pattern of orbit drift (Fig. 3). For instance, Landsat 7's orbit is drifting gradually, which is different from the irregular and fluctuating orbit change of Landsat 5. Moreover, Landsat 7 will drift toward a much earlier mean local acquisition time in the near future, but Landsat 5 has not collected data of similar conditions as it was decommissioned before it was moved to a lower orbit. On the other hand, the Earth Observing-1 (EO-1) satellite carried onboard an Advanced Land Imager (ALI) multispectral sensor similar to that of Landsat 7, and was launched on November 21, 2000. After EO-1 expended all maneuvering fuel in 2011, its orbit began to drift steadily until all the way to 8:00 a.m. mean local time. This study provides firsthand data on how Landsat 7 observations will be influenced when its orbit drifts much earlier (black dots in Fig. 2).

While it is important to quantify and predict the impact of Landsat 7's orbit drift on its observations, what is more critical is to test methods for correcting the orbit drift artifact of Landsat 7 observations to

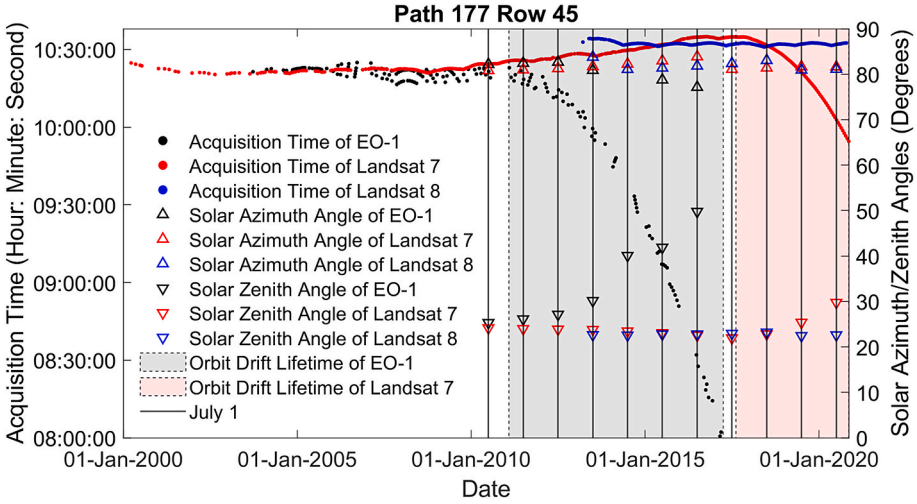

Fig. 2. Local acquisition time (left y-axis) and solar angles (right y-axis) of EO-1, Landsat 7, and Landsat 8 for images collected at Worldwide Reference System Two (WRS-2) Path 177/Row 45 (Center Latitude/Longitude: 21.6742/28.2286). EO-1's orbit started to drift in February 2011 and ended in March 2017 (grey area). Landsat 7's orbit started to drift in August 2017 (red area). The mean local acquisition time (without orbit drift) of EO-1, Landsat 7, and Landsat 8 is 10:21 a.m., 10:26 a.m., and 10:32 a.m., respectively. The solar azimuth/zenith angles are derived from the satellite observations in the growing season of each calendar year (the closest acquisition date to July 1). Observations from Landsat 7 and 8 acquired in the growing season of 2018, 2019, and 2020 are compared for quantifying the effect of ongoing Landsat 7's orbit drift, and observations between EO-1 and Landsat 7 from 2010 to 2016 are used for estimating the effect of future Landsat 7's orbit drift. The orbit status of EO-1 in 2012 and 2013 are similar to that of Landsat 7 in 2019 and 2020, and the future Landsat 7 orbit between 2021 and 2023 can be inferred from EO-1 orbit between 2014 and 2016. This Path/Row is selected as it contains a large number of EO-1 observations, and this figure is created based on the metadata from each sensor collected from January 1, 2000 to November 14, 2020. (For interpretation of the references to colour in this figure legend, the reader is referred to the Web version of this article.)

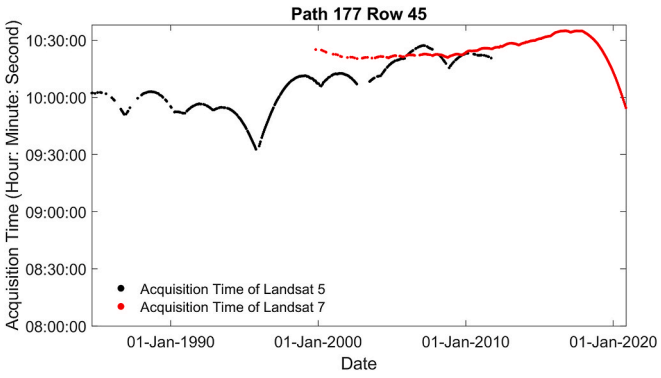

Fig. 3. Comparison of the local acquisition time between Landsat 5 and Landsat 7 images collected at Worldwide Reference System Two (WRS-2) Path 177/Row 45 (Center Latitude/Longitude: 21.6742/28.2286). Landsat 5 orbit was changed from 1995 to 2000, and from 2003 to 2007 by irregular station keeping maneuvers, while Landsat 7 orbit is gradually drifting due to limited fuel resources. Note that Landsat 5 was decommissioned due to the failure of a redundant gyroscope and thus it did not collect any data under the gradually drifting orbit like Landsat 7.

preserve its science capability for quantitative remote sensing (Goward et al., 2001). The impact of Landsat 7's orbit drift is essentially a BRDF problem, in which the reflected energy received by the sensor's viewing angle changes in response to higher solar zenith angles. Thus, BRDF models provide a viable method to correct orbital drift artifacts to pre-drift solar illumination angles. The RossThick-LiSparse-Reciprocal model (Li and Strahler, 1992; Ross, 1981; Roujean et al., 1992) is one of the most widely used BRDF models, and based on this model, BRDF normalization has been well studied for the MODerate Resolution Imaging Spectroradiometer (MODIS) data with sequential multiangle observations (Schaaf et al., 2002). For Landsat data, however, all observations are collected at similar solar and sensor viewing angles, and thus there is no way to solve the parameters of the BRDF model. One alternative is to use a c-factor BRDF normalization approach to correct Landsat BRDF effects based on the predefined global MODIS BRDF product (Roy et al., 2016). This approach has been proven to be accurate for reducing the BRDF effects from sensor viewing angle differences (Claverie et al., 2018), but has not been tested for scenarios where solar angles show large differences. Thus, this study is concerned with evaluating whether this c-factor BRDF normalization approach could be useful for reducing the effect of Landsat 7's orbit drift that is mostly contributed by solar angle changes.

In this study, we will focus on 1) quantifying the effect of Landsat 7's ongoing orbit drift by comparing it to that of Landsat 8, 2) testing the c-factor BRDF normalization approach for reducing the orbit drift effects dominated by solar angle changes, and 3) estimating the effect of Landsat 7's future orbit drift based on historical EO-1 data.

The rest of this paper is organized as follows. Study area and data will be introduced in Section 2, followed by the methods in Section 3. Section 4 describes the results of analyzing the effect of Landsat 7's orbit drift. Discussions are presented in Section 5, and Section 6 delivers the conclusions.

2. Study area and data

To explore the effect of Landsat 7's orbit drift, we compared orbit drifting Landsat 7 data collected between 2018 and 2020 with Landsat 8 data in a nominal orbit collected at the nearly same time (as reference). On the other hand, considering EO-1 and Landsat 7 share a similar orbit drifting trajectory (except that EO-1 occurred earlier), we used EO-1 data collected between 2010 and 2016 to simulate future Landsat 7 observations with orbit drift and compared that with Landsat 7's nominal orbit. Note that the EO-1 satellite had both Hyperion and ALI instruments onboard, and this study uses the ALI data only. Fig. 4 illustrates the similar spectral bands between Landsat 7, Landsat 8, and EO-1. We used the observations collected during the growing season of each year (July 1 ± 30 days) across the Northern Hemisphere (0–75^0 N) terrestrial areas for our analysis (Fig. 5), as growing season observations are less likely to be influenced by snow/ice and are used more often in remote sensing applications (Ju and Masek, 2016; Pflugmacher et al., 2014; Vicente-Serrano et al., 2008). Besides, we also analyzed the orbit drift effect on Landsat 7 observations for different kinds of land cover types, as different land cover may respond differently.

2.1. Landsats 7–8 observations collected between 2018 and 2020

To better understand the effect of orbit drift on the current Landsat 7 data, we compared Collection 1 surface reflectance and Top-Of-Atmosphere (TOA) reflectance of growing season observations (July 1 ± 30 days) between Landsat 7 with orbit drift and Landsat 8 in normal orbit in 2018, 2019, and 2020, based on 10,000 pixels randomly collected within the Northern Hemisphere (0–75^0 N) terrestrial areas (Fig. 5). According to GlobeLand30 land cover product (see Section 2.3 for details), these observations consisted 13.83% cultivated land, 26.67% forest, 19.31% grassland, 4.66% shrubland, 2.77% wetland, 3.94% water, 10.57% tundra, 1.00% artificial surfaces, 14.51% bareland, and 2.74% permanent snow/ice. We downloaded Collection 1 surface reflectance, TOA reflectance, and Quality Assessment (QA) products for Landsat 7 and Landsat 8 located at the same pixels from Google Earth Engine (Gorelick et al., 2017). Note that the surface reflectance and TOA reflectance products were generated by Google, and the QA band was generated by USGS and redistributed by Google. The surface reflectance data for Landsat 7 and 8 were produced using the Landsat Ecosystem Disturbance Adaptive Processing System (LEDAPS) version 3.2.1 (Masek et al., 2006) and the Landsat Surface Reflectance Code (LaSRC) version 1.3.0 (Vermote et al., 2016), respectively. The generation of the TOA reflectance data for Landsat 7 and Landsat 8 was based on Chander et al. (2009) and the calibration coefficients were extracted from the image metadata. The QA band of Landsat 7 and Landsat 8 can provide the mask of cloud, cloud shadow, and snow/ice, which was generated by USGS using the C version of Function of mask (Fmask) algorithm version 3.2 (Foga et al., 2017; Zhu et al., 2015; Zhu and Woodcock, 2012). To avoid the influences of the sensor view angle difference from adjacent orbits (±7.5°), we only used the observations from the same Landsat orbit path in our analyses.

2.2. EO-1 and landsat 7 observations collected between 2010 and 2016

Landsat 7's orbit started to drift since its last inclination maneuver on August 12, 2017, although the orbit drift before 2017 is negligible relative to the nominal orbit requirement (red dots in Fig. 2). EO-1 experienced similar orbit drift as what Landsat 7 does, but it started from February 2011 until the end of its lifetime in March 2017. Therefore, we collected TOA reflectance of growing season observations (July 1 ± 30 days) from EO-1 images with orbit drift and Landsat 7 images in its nominal orbit within the same Northern Hemisphere (0–75^0 N) terrestrial areas between 2010 and 2016 to estimate the effect of Landsat 7's future orbit drift.

EO-1 collected narrow swath images with a width of 27 km over the same Landsat Path/Row Worldwide Reference System Two (WRS-2) orbital track, but it only collected observations over certain parts of the world on purpose because it was a demonstration rather than an operational mission (see blue footprints in Fig. 5). EO-1 has acquired images over lots of targeted areas around the world, which were predetermined in the first year of the mission (in 2001) and later collected within customer requested areas for the remaining mission duration between 2002 and 2017. EO-1 had the pointing capability to observe the target areas from the nadir and/or off-nadir swaths (neighboring west and east paths). To ensure the consistency of view angles of EO-1 and Landsat

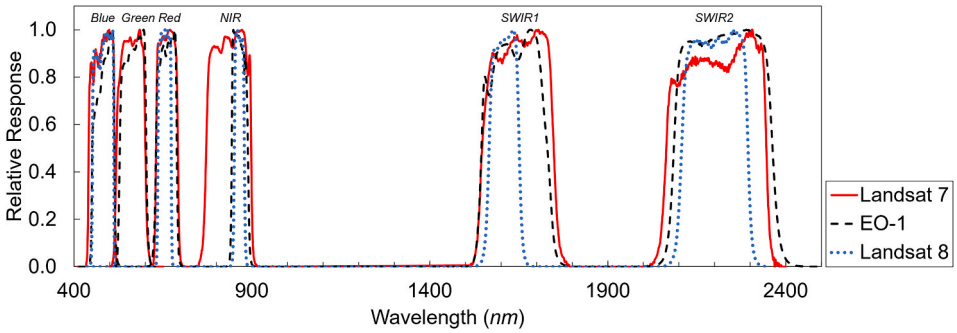

Fig. 4. Spectral response functions of Landsat 7 ETM+, Landsat 8 Operational Land Imager (OLI), and EO-1 ALI. Only observations from the six spectral bands plotted here are analyzed. The relative response functions were obtained from USGS (https://landsat.usgs.gov/spectral-characteristics-viewer; Last access on April 17, 2021).

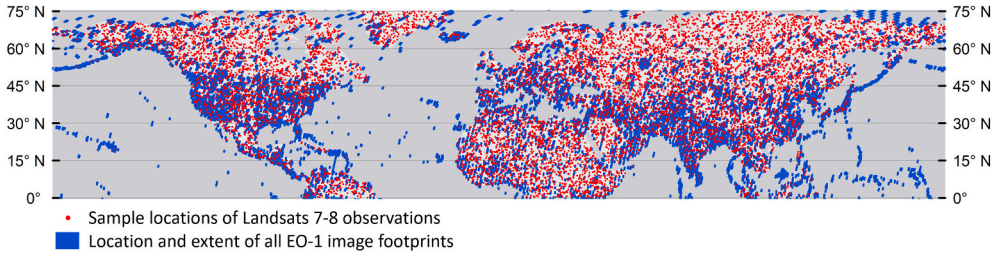

Fig. 5. Distribution of sample data across the Northern Hemisphere (0–75^0 N) terrestrial areas. The red dots show the sample locations of Landsats 7–8 observations collected between 2018 and 2020 for studying the effect of ongoing Landsat 7's orbit drift. The blue rectangles show the location and extent of all EO-1 image footprints for estimating the effect of future Landsat 7's orbit drift. (For interpretation of the references to colour in this figure legend, the reader is referred to the Web version of this article.)

images (nadir to ± 7.5°), we only used the images observed from the nadir path. All EO-1 images at Level-1T Digital Value (DN) with less than 80% cloud cover were downloaded from USGS and converted to TOA reflectance based on Chander et al. (2009). Within the same scanned areas (Path/Row) from EO-1, we downloaded the corresponding Landsat 7 Collection 1 Level-1T images collected between 2010 and 2016 from USGS and converted them to TOA reflectance as what we did for EO-1 (Chander et al., 2009). We did not convert EO-1 data to surface reflectance for this analysis mainly because EO-1 is a pathfinder satellite and there is no operational atmospheric compensation algorithm or derived Level 2 product that is provided for the globe at the time of this study.

2.3. Land cover data

The land cover data were derived from 2010 GlobeLand30 (Chen et al., 2015). It provides maps at 30-m resolution and a total of 10 land cover classes, such as cultivated land, forest, grassland, shrubland, wetland, water, tundra, artificial surface, bareland, and permanent snow/ice. We analyzed all land cover classes, except for snow/ice in this study. The ocean pixels labeled in this product were also excluded from our analysis.

3. Methods

3.1. Data pre-processing

For optical remote sensing data such as Landsat and EO-1, clouds, cloud shadows, and snow/ice need to be screened during image processing (Zhu et al., 2018). As for Landsat 7 and 8, we used the QA band to screen out the noise (e.g., clouds, cloud shadows, and snow/ice) for each pixel. Since EO-1 has neither thermal nor cirrus spectral bands, we modified the Fmask algorithm (version 4.0) designed for Sentinel-2 data (which also does not have a thermal infrared band) to identify clouds, cloud shadows, and snow/ice in EO-1 images (Qiu et al., 2019). All modules and tests were used except for the ones that involve the use of cirrus band. Pixel observations with reflectance less than 0 or larger than 1 were also excluded. Finally, the growing season data of each year were composited by selecting the clear observations (not cloud, cloud shadow, or snow) closest to July 1, within 30 days.

3.2. Metrics for analyzing orbit drift effect

We quantified the effect of Landsat 7's orbit drift on the six widely used multispectral bands (e.g., Blue, Green, Red, NIR, SWIR1 and SWIR2 bands) as well as NDVI by comparing the growing season observations collected in the Northern Hemisphere terrestrial areas (Fig. 5). The effects on spectral bands were estimated based on the median value of reflectance differences between the satellite with obit drift and the satellite in a nominal orbit (Eqs. (1)–(3)). For each pixel and for each study year, we calculated the surface reflectance difference ($\Delta\rho_{sr}$) and the TOA reflectance difference ($\Delta\rho_{toa}$) of the growing season observation between Landsat 7 with orbit drift and Landsat 8 its nominal orbit, and the TOA reflectance difference ($\Delta\rho_{toa}$) between EO-1 with orbit drift and Landsat 7 in its nominal orbit (Eq. (3)). The median value of the reflectance differences of all sample data ($median\ \Delta\rho_{sr}$ or $median\ \Delta\rho_{toa}$) was used for quantifying the orbit drift effect for each year (Eq. (2)). Besides the orbit drift, the systematic difference between the sensors, such as the bandpass difference (Fig. 4), could also contribute to the reflectance difference. To solely focus on the impact of orbit drift (d), we used the median value of the reflectance differences between two satellites when one of them was having a drifting orbit minus the median value when both of them were in a nominal orbit (Eq. (1)), assuming systematic sensor difference from sensors would be removed in the latter values. In addition, following the similar metrics, we also estimated the orbit drift effect on NDVI derived from surface reflectance ($NDVI_{sr}$) or that from TOA reflectance ($NDVI_{toa}$) based on the median value of the NDVI differences of all sample data ($median\ \Delta NDVI_{sr}$ or $median\ \Delta NDVI_{toa}$) (Eqs. (1)–(3)).

$$d(t) = median\ \Delta\rho\ (t) - median\ \Delta\rho\ (t_0) \quad (1)$$

$$median\ \Delta\rho\ (t) = median\ \{\Delta\rho_1(t), \Delta\rho_2\ (t), \Delta\rho_3\ (t), \ldots,\ \Delta\rho_n\ (t)\} \quad (2)$$

$$\Delta\rho_i\ (t) = \overline{\rho}_i(t) - \rho_i(t) \quad (3)$$

where,

d is the orbit drift effect indicator,

$\Delta\rho$ is the reflectance (or NDVI) differences between the satellite with orbit drift and the satellite in nominal orbit,

$median\ \Delta\rho$ is the median value of $\Delta\rho$ of all sample pixels,

$\overline{\rho}$ is the growing season reflectance of spectral band (or NDVI) of the satellite with orbit drift,

ρ is the growing season reflectance of spectral band (or NDVI) of the satellite in nominal orbit,

t is the study year (e.g., 2018–2020 for Landsat 7 and 2010–2016 for EO-1),

t_0 is the year in which both two satellites are in a nominal orbit (e.g., 2018 for comparing Landsat 7 and 8; 2010 for comparing EO-1 and Landsat 7),

i is the ith sample pixel,

n is the total number of sample pixels.

For instance, in order to study the effect of the ongoing Landsat 7's orbit drift, we plotted the histogram of growing season surface reflectance difference values ($\Delta\rho_{sr}$) and their derived NDVI difference values ($\Delta NDVI_{sr}$) between Landsat 7 and Landsat 8 for 2018, 2019, and 2020 (Fig. 6). Even though Landsat 7 started to drift in 2017, its acquisition time was slightly later than Landsat 8 in 2017, and they shared a very close acquisition time in 2018 (Fig. 2). Thus, the $median\ \Delta\rho_{sr}$ (2018) (or $median\ \Delta NDVI_{sr}$ (2018)) can still be considered as the indicator that represents the systematic sensor difference, and the orbit drift effect can be estimated by subtracting them from the $median\ \Delta\rho_{sr}$ (or $median\ \Delta NDVI_{sr}$) in other study years (Eq. (1)). For example, with $median\ \Delta\rho_{sr}(2019) - median\ \Delta\rho_{sr}(2018)$ and $median\ \Delta\rho_{sr}(2020) - median\Delta\rho_{sr}(2018)$, we were able to respectively quantify the effect of Landsat 7's orbit drift on surface reflectance in 2019 and 2020. If the final drift effect indicator (e.g., d_{sr} or $d_{NDVI_{sr}}$) was less than 0 (Eq. (1)), the orbit drift would lead to a decrease of surface reflectance or its NDVI, and vice versa. The same approach was utilized to assess the effect of the Landsat 7's orbit drift on the TOA reflectance of each spectral band and their derived NDVI values (e.g., d_{toa} and $d_{NDVI_{toa}}$).

To estimate the effect of future Landsat 7's orbit drift, we compared the EO-1 and the Landsat 7 growing season TOA reflectance and the corresponding NDVI values ($NDVI_{toa}$) from 2010 to 2016. The $median\ \Delta\rho_{toa}(2010)$ (or $median\ \Delta NDVI_{toa}(2010)$) was selected for representing the systematic sensor difference between EO-1 and Landsat 7, because of their similar acquisition time in 2010 (Fig. 2). EO-1 started to drift in 2011, but we observed that the acquisition time difference caused by orbit drift between EO-1 and Landsat 7 in 2012 and 2013 was more like that between Landsat 7 and Landsat 8 in 2019 and 2020 (Fig. 2). Therefore, the orbit drift effect d_{toa} (or $d_{NDVI_{toa}}$) of EO-1 between 2014 and 2016 could simulate the effect of the future Landsat 7's orbit drift between 2021 and 2023.

3.3. BRDF normalization

The c-factor BRDF normalization approach (Roy et al., 2016) was applied for reducing the orbit drift effect, and the nadir surface reflectance was calculated by Eq. (4), in which the parameters were empirically estimated based on the global MODIS 500-m BRDF parameter product (Schaaf et al., 2002). The optimal normalized solar zenith angle was determined for each location based on a sixth-degree polynomial

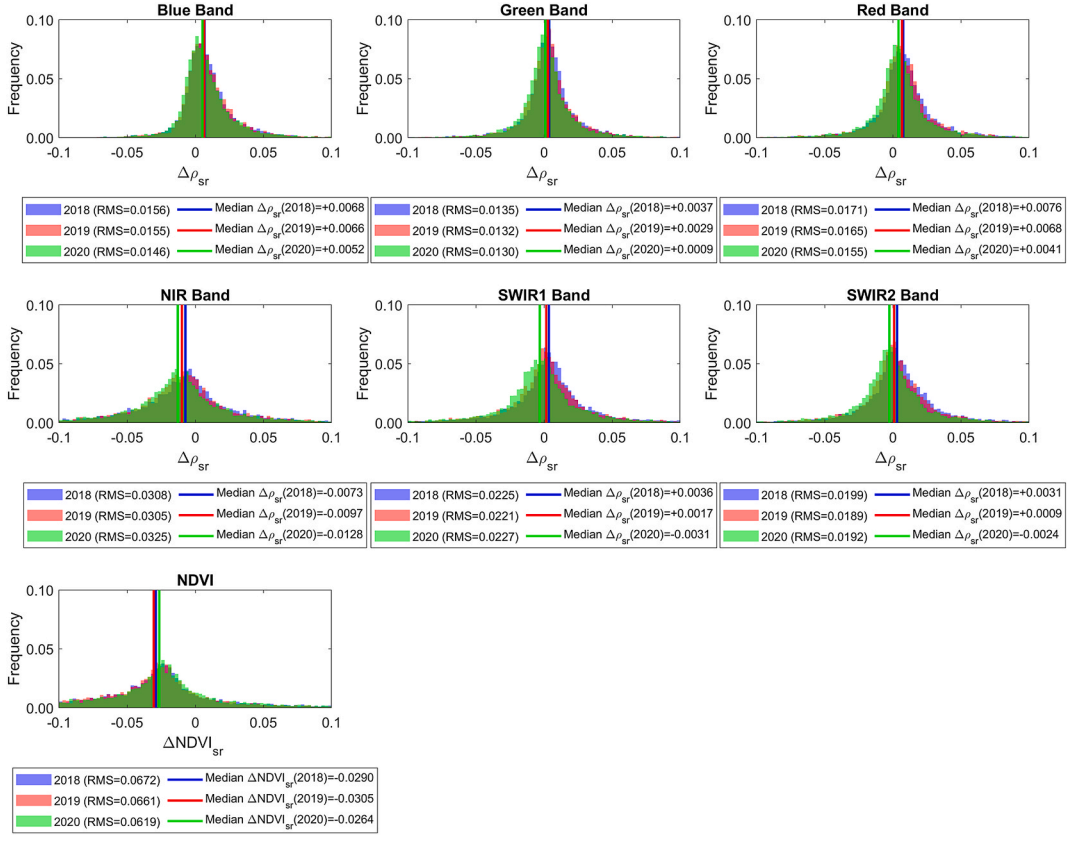

Fig. 6. Histogram of the surface reflectance difference values ($\Delta\rho_{sr}$) of each spectral band and their derived NDVI difference values ($\Delta NDVI_{sr}$) between Landsat 7 and Landsat 8 in 2018, 2019, and 2020. The median value (blue lines) in 2018 indicates the systematic difference between the two sensors. The effect of orbit drift can be quantified based on the distance between the 2019 or 2020 median values (red or green lines) and 2018 median values (blue lines) (Eq. (1)). (For interpretation of the references to colour in this figure legend, the reader is referred to the Web version of this article.)

function of the latitude (η) (Eq. (5)) (Zhang et al., 2015). This c-factor normalization method was applied to correct the BRDF of all Landsat 7 and Landsat 8 surface reflectance data in 2019 and 2020, and then we also calculated the reflectance difference between the normalized Landsat 7 and Landsat 8 data as we described in Section 3.2.

$$\rho^{'} = \rho \cdot \frac{f_{iso} + f_{vol} \cdot K_{vol}(\theta^{'}, 0^{\circ}, \varphi) + f_{geo} \cdot K_{geo}(\theta^{'}, 0^{\circ}, \varphi)}{f_{iso} + f_{vol} \cdot K_{vol}(\theta, \varnothing, \varphi) + f_{geo} \cdot K_{geo}(\theta, \varnothing, \varphi)} \quad (4)$$

$$\theta^{'} = 31.0076 - 0.1272 \cdot \eta + 0.01187 \cdot \eta^2 + 2.4 \times 10^{-5} \cdot \eta^3 - 9.48 \times 10^{-7} \cdot \eta^4 - 1.95 \times 10^{9} \cdot \eta^5 + 6.15 \times 10^{-11} \cdot \eta^6 \quad (5)$$

where,

$\varnothing$ is the view zenith angle,

φ is the view-sun relative azimuth angle,

θ is the solar zenith angle,

$\theta^{'}$ is the normalized solar zenith angle that can be calculated by Eq. (5),

ρ is the original reflectance,

$\rho^{'}$ is the BRDF normalized reflectance at nadir,

f_{iso}, f_{vol}, and f_{geo} are the BRDF model parameters derived from MODIS product (Schaaf et al., 2002),

K_{vol} and K_{geo} are the RossThick kernel (Ross, 1981) and the LiSparse kernel (Li and Strahler, 1992), respectively,

η is the latitude of Landsat pixel.

4. Results

4.1. Effect of ongoing landsat 7's orbit drift

Fig. 7a and b illustrate the effect of Landsat 7's orbit drift on each spectral band and NDVI values in 2019 and 2020. The Landsat 7's orbit drift generally decreased the surface reflectance as well as the TOA reflectance in 2019 and 2020, and the effect in 2020 is more severe. Generally, the effects of orbit drift on the surface reflectance and the TOA reflectance were more substantial for SWIR1 (maximum effect), SWIR2, and NIR bands, and less for the visible bands such as Red, Green, and Blue (minimum effect) bands. The overall effects on both surface reflectance and TOA reflectance were small in 2019 and 2020 in that the spectral bands have shown a surface reflectance change from - 0.0001 (Blue band in 2019) to - 0.0067 (SWIR1 band in 2020) and a TOA reflectance change from - 0.0005 (Blue band in 2019) to - 0.0069 (SWIR1 band in 2020). The surface reflectance derived NDVI ($NDVI_{sr}$) and TOA reflectance derived NDVI ($NDVI_{toa}$) values also shared a similar limited effect caused by the orbit drift, which presented an increase in 2020 (e.g., +0.0026 in $NDVI_{sr}$ and +0.0022 in $NDVI_{toa}$), even though a little decrease in 2019 was observed (e.g., −0.0015 in $NDVI_{sr}$ and −0.0009 in $NDVI_{toa}$). Note that since NDVI is a ratio between NIR and Red bands, the decreases in both NIR and Red bands cannot ensure NDVI always increases especially when the orbit drift impact is very limited. The orbit drift effects can vary a lot depending on different land cover types (Fig. 8). For example, the shrubland was mostly impacted by the orbit drift, with a surface reflectance decrease of more than 0.01 in both NIR and SWIR1 bands. The NDVI values of water and wetland were easily influenced, since their NIR and Red bands were relatively small and any variations in the two bands would result in a large difference in NDVI.

Compared to the results derived from the original data (Fig. 7a), the c-factor BRDF normalization could substantially reduce the orbit drift effects on the surface reflectance, with a smaller drift effect indicator (d_{sr}) for each spectral band in 2019 and 2020 (Fig. 7c). The detailed benefits for different kinds of land cover types could be found by comparing Fig. 9 and Fig. 8, where smaller drift effects (d_{sr}) were observed in most of the land cover types and the absolute values in almost all spectral bands and land cover types were less than 0.005. In addition, though the overall effect of Landsat 7's orbit drift on NDVI decreased slightly in 2020 (+0.0012 vs. +0.0026 in $NDVI_{sr}$) (Fig. 7c vs. Fig. 7a), the c-factor BRDF normalization did not significantly reduce the effects for different kinds of land cover types (Fig. 9 vs. Fig. 8). This result was expected since the NDVI ratio formulation between Red and NIR bands has already reduced the sensitivity to BRDF effects (Gao et al., 2002; Zhang et al., 2018).

4.2. Effect of future landsat 7's orbit drift

Fig. 10 shows the effect of EO-1's orbit drift on the TOA reflectance of each spectral band and their derived NDVI values ($NDVI_{toa}$) from 2012 to 2016, which could be used for simulating the effect of Landsat 7's orbit drift in the future. The orbit drift effect values (d_{toa} and $d_{NDVI_{toa}}$) in 2014, 2015, and 2016 for EO-1 were used as the proxy for the effect of future Landsat 7's orbit drift in 2021, 2022, and 2023, according to their similar orbit conditions (Fig. 2). It is apparent that Landsat 7's orbit drift would continuously decrease the TOA reflectance for all bands, and compared to the visible bands, the NIR and two SWIR bands would be influenced more by the orbit drift. In this analysis, the orbit drift effects on NDVI were not consistent year by year, which is mainly because EO-1 only observed the Earth's surface over certain parts of the world and its coverage could be quite different on a yearly basis. However, we can still observe the increasing patterns in NDVI. For 2021 (corresponding to 2014 EO-1 data) and beyond, the overall TOA reflectance of Green and Red bands will decrease more than 0.005 (absolute d_{toa}). NIR and SWIR bands will be decreased at a level of around 0.015.

5. Discussions

Landsat 7 has collected more than two decades of data for monitoring terrestrial areas with high radiometric and geometric consistency (Goward et al., 2001; Schott et al., 2016). However, since 2017, its orbit has been gradually drifting to an earlier mean local acquisition time, and the meaningful drift impact was observed for the first time in 2019

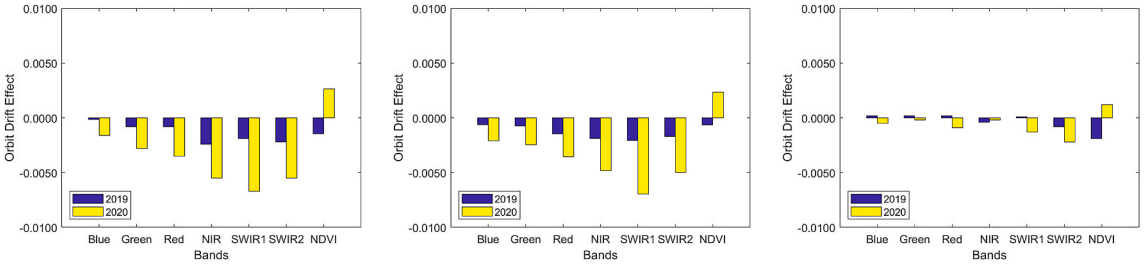

Fig. 7. Effect of Landsat 7's orbit drift in 2019 and 2020. (a) Surface reflectance of spectral bands and their derived NDVI values. (b) TOA reflectance of spectral bands and their derived NDVI values. (c) BRDF normalized surface reflectance of spectral bands and their derived NDVI values. The orbit drift effect (y-axis) in (a) and (c) indicates d_{sr} or $d_{NDVI_{sr}}$, and the orbit drift effect (y-axis) in (b) indicates d_{toa} or $d_{NDVI_{toa}}$, which were evaluated by comparing Landsat 7 with orbit drift and Landsat 8 in normal orbit (Eq. (1)).

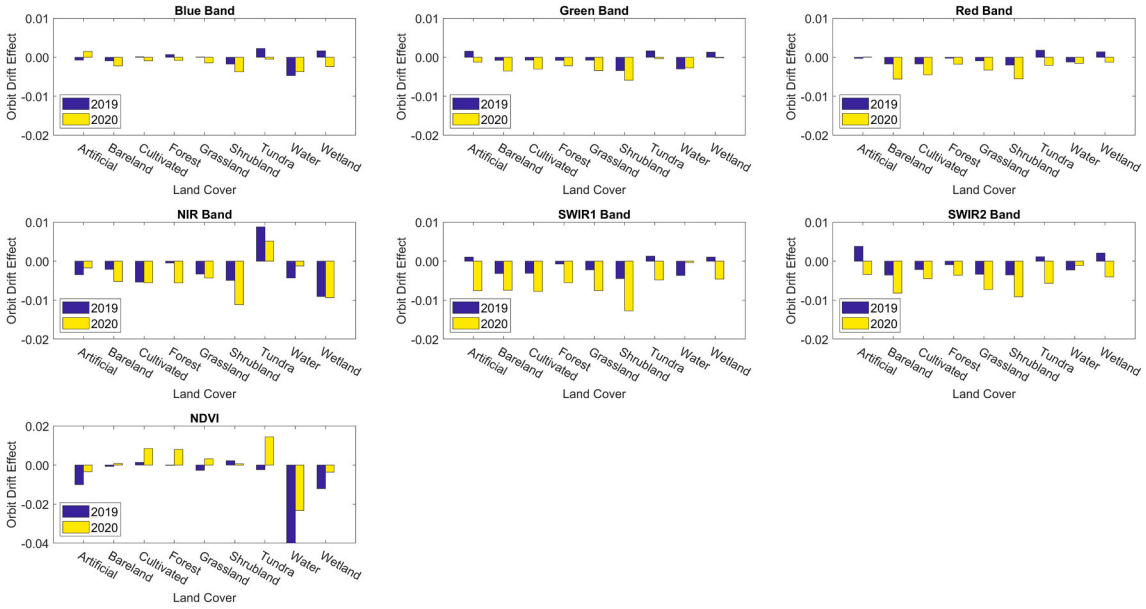

Fig. 8. Effect of Landsat 7's orbit drift on the surface reflectance for different kinds of land cover types in 2019 and 2020. The orbit drift effect in y-axis indicates d_{sr} for surface reflectance or $d_{NDVI_{sr}}$ for surface reflectance derived NDVI, which were evaluated by comparing Landsat 7 with orbit drift and Landsat 8 in normal orbit (Eq. (1)).

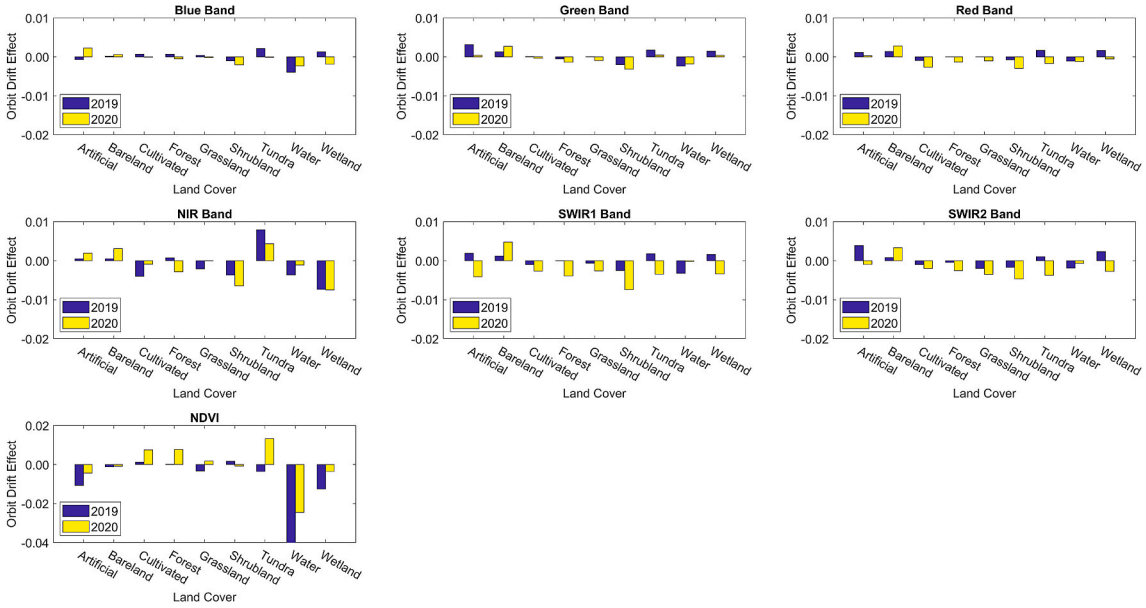

Fig. 9. Effect of Landsat 7's orbit drift on the BRDF normalized surface reflectance for different kinds of land cover in 2019 and 2020. The orbit drift effect in y-axis indicates d_{sr} for spectral band and $d_{NDVI_{sr}}$ for surface reflectance derived NDVI, which were evaluated by comparing Landsat 7 with orbit drift and Landsat 8 in nominal orbit (Eq. (1)).

(Fig. 2). Even though Landsat 8 is operating nominally at the current time, to preserve the use of Landsat 7 data and maintian the two Landsat observatory operational concept (e.g., 8 revisit days for two Landsat satellites) is important, particularly through the successful launch and commissioning of Landsat 9 in late 2021 (Masek et al., 2020). In this study, we examined the impact of orbit drift on visible to shortwave infrared multispectral bands and their derived NDVI values by comparing the growing season observations (July 1 $\pm$ 30 days) from Landsat 7 with orbit drift and that from Landsat 8 in a nominal orbit using a total of 10, 000 pixels randomly selected over the Northern Hemisphere terrestrial areas. It was observed that the orbit drift generally decreases the measured reflectance value of all spectral bands, but its influence varies among the bands, with the impacts decreasing in the order of SWIR1, SWIR2, NIR, Red, Green, and Blue of surface and TOA reflectance bands. The mechanism for decreasing reflectance could be explained by the resulting increase in the solar zenith angle, which leads to a longer radiance transfer path from sun to surface to sensor (Franks et al., 2017; Swinnen et al., 2014) and increases the amount of shadowing simultaneously (e.g., tree shadows, built-up shadows, and terrain shadows) (Dare, 2005; Giles, 2001; Ranson and Daughtry, 1987). We also observed that surface reflectance and TOA reflectance derived NDVI values generally increases with the orbit drift in 2020, which agrees with findings in other orbit drift studies (Gao et al., 2002; Roy et al., 2020; Zhang and Roy, 2016). In 2019 and 2020, however, the

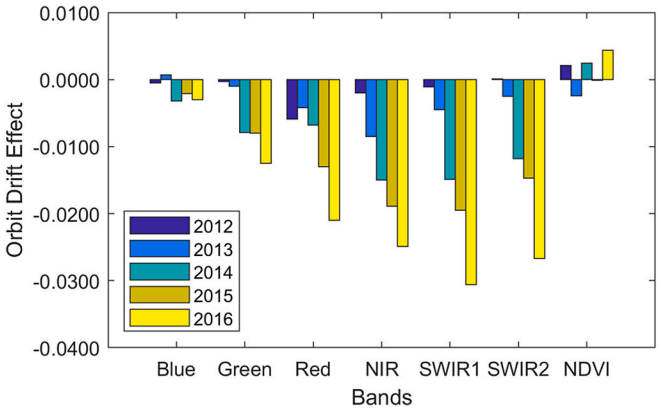

Fig. 10. Effect of EO-1's orbit drift on the TOA reflectance from 2012 to 2016. The orbit drift effects in y-axis indicates d_{toa} for spectral band and $d_{NDVI_{toa}}$ for TOA reflectance derived NDVI, which were evaluated based on the comparison between EO-1 with orbit drift and Landsat 7 in normal orbit (Eq. (1)).

overall effects on surface reflectance, TOA reflectance, and their derived NDVI values were relatively small. This is because the Landsat 7's orbit did not change too much until July 2020, with ~40 min earlier in mean local acquisition time and ~8° higher in solar zenith angle (Fig. 2). For instance, the range of the surface reflectance change, caused by the Landsat 7's orbit drift, could vary from −0.0001 (Blue band in 2019) to −0.0067 (SWIR1 band in 2020), and the TOA reflectance could vary from −0.0005 (Blue band in 2019) to −0.0069 (SWIR1 band in 2020) (Fig. 7). Considering that the internal overall uncertainties of Landsat 7 surface reflectance product vary from 0.005 to 0.01 depending on the spectral bands (Claverie et al., 2015), we suggest that for Landsat 7 data collected before the growing season in 2020, the effect of orbit drift is within the known uncertainty range, and the data can be used for most quantitative remote sensing analysis without any additional processing. However, it is worthwhile to note that for specific land cover types, such as bareland, cultivated, forest, grassland, and shrubland, relatively larger differences (absolute $d_{sr} > 0.005$ or 0.01) were observed for NIR and SWIR bands in 2020 (Fig. 8), and thus should be given particular attention if Landsat 7 data are used for application on certain land cover types and specific Landsat spectral bands.

The growing season (summer) data were used to analyze the effect of Landsat 7's orbit drift in this study, considering that they are used more often in remote sensing applications with less snow/ice influences (Ju and Masek, 2016; Pflugmacher et al., 2014; Vicente-Serrano et al., 2008). At the same time, we also observed that the overall effects on each spectral band and their derived NDVI values in summer were greater than that in the other three seasons (i.e., winter, spring, and autumn) (Fig. 11). This is mainly because the orbit drift effect is a BRDF problem, and in summer vegetation such as forest and shrubland, with leaf out and various canopy structures, would be more sensitive to BRDF effects (Sims et al., 2011). In addition, the effects in spring are slightly higher than that in autumn for most of the spectral bands except for Green, SWIR2, and NDVI bands. Winter also presented a comparable effect with spring and autumn, mainly because of the high solar zenith angle (Wang et al., 2014).

Though Landsat 7 thermal infrared (TIR) data are less used than the six visible to shortwave infrared bands, it is still interesting to evaluate the impact of orbit drift effect on the single TIR spectral band. Therefore, we analyzed Brightness Temperature (BT) of the single TIR band by comparing Landsat 7 with orbit drift and Landsat 8 in a nominal orbit over the same sample pixels as did for spectral bands (Fig. 12). It is observed that the BT of Landsat single TIR band decreased gradually from 2018 to 2020, but the effect so far is still limited. For example, the effect in 2020 generally decreased the BT by 0.12 ^{o}C, which is calculated by $median\ \Delta BT_{sr}(2020) - median\ \Delta BT_{sr}(2018)$. Landsat 7 science and

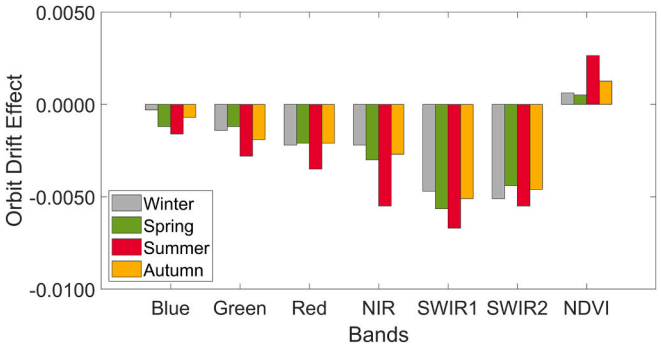

Fig. 11. Comparisons of Landsat 7's orbit drift effects on surface reflectance and their derived NDVI in winter, spring, summer, and autumn in 2020. The orbit drift effects in y-axis indicates d_{sr} for surface reflectance of spectral band and $d_{NDVI_{sr}}$ for surface reflectance derived NDVI, which were evaluated based on comparison between Landsat 7 with orbit drift and Landsat 8 in normal orbit (Eq. (1)). January 1, April 1, July 1, and October 1 were selected corresponding to winter, spring, summer, and autumn in Northern Hemisphere terrestrial areas, respectively. Since the Landsat 7's orbit is always drifting, the orbit in autumn drifts more compared to summer, but winter and spring, less.

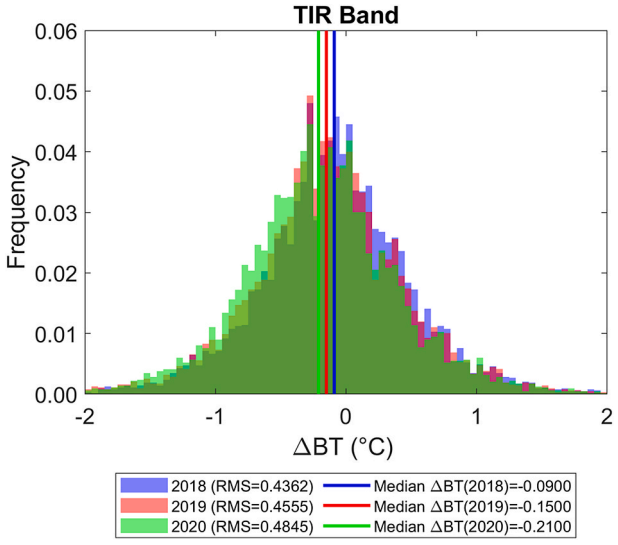

Fig. 12. Histogram of the Brightness Temperature (BT) difference values of TIR band (ΔBT) between Landsat 7 and Landsat 8 in 2018, 2019, and 2020. TIR band of Landsat 7 is in the 10.40–12.50 μm wavelengths, and that of Landsat 8 at 10.6–11.19 μm. The median value (blue lines) in 2018 indicates the systematic difference between the two sensors. The effect of orbit drift on Landsat 7's BT can be quantified based on the distance between the 2019 or 2020 median values (red or green lines) and 2018 median values (blue lines). (For interpretation of the references to colour in this figure legend, the reader is referred to the Web version of this article.)

applications that utilize the single TIR band such as urban heat island (Weng et al., 2004), inland water and coastal ocean (Wloczyk et al., 2006), and evapotranspiration estimation (Anderson et al., 2012; Yang et al., 2020) should also observe orbit drift TIR effects within the known range of uncertainty prior to 2020. Since the EO-1 has no TIR band, we cannot predict the future effects, but we expect that the effects would be larger because an earlier mean local acquisition time resulting in lower observed temperatures.

The c-factor BRDF normalization approach is based on the MODIS BRDF product (Roy et al., 2016), which means the BRDF shapes will be transferred from MODIS to Landsat. Considering the spatial resolution of MODIS (500 m) is much coarser than Landsat, the direct use of BRDF shapes from MODIS may not be optimal for Landsat data, particularly for

heterogeneous areas where MODIS pixel is easily mixed by different kinds of cover types. For the current small variation of solar angles (e.g., ~8° in solar zenith angle), the c-factor approach may still be a good approximation, but when Landsat 7's orbit drifts further with larger variations in solar angles, other methods for deriving BRDF curves based on land cover types selected from large pure MODIS pixels may provide better results (Shuai et al., 2014).

In the future, the effects of Landsat 7's orbit drift will become more severe after 2021, according to the historical EO-1 data (Fig. 10). Fig. 13 shows a time series of TOA reflectance data from Landsat 7 and EO-1 between 2010 and 2016. As time went on, the orbit drift effect was more severe in each spectral band, and subsequently the time series consistency of EO-1 data was influenced as well. Therefore, removing artifact from the orbit drift is highly recommended for remote sensing applications that need accurate post-2021 Landsat 7 reflectance values, such as vegetation greenness trend analyses (Ju and Masek, 2016; Sulla-Menashe et al., 2018; Zhou et al., 2014; Zhu et al., 2016) and land surface change detection (Brown et al., 2020; DeVries et al., 2015; Kennedy et al., 2010; Zhu and Woodcock, 2014). However, applications such as topographic correction (Gu and Gillespie, 1998; Tan et al., 2013) or retrieval of vegetation biophysical parameters based on physical models (Jacquemoud et al., 2009; Verhoef, 1984), which already considers solar and view geometries, may have very limited impacts. In this study, we only used the historical EO-1 data with orbit drift to estimate the effects of Landsat'7 orbit drift, which may not represent the true orbit drift impact from future Landsat 7 observations. We will continue to evaluate and update Landsat 7's orbit drift impact on real Landsat 7 data in the future, and results will be updated at: https://github.com/GERSL/L7drift.

6. Conclusions

The orbit of Landsat 7 began to drift to an earlier mean local acquisition time since 2017. According to the analysis of the growing season terrestrial surface observations within the Northern Hemisphere, we observed that the orbit drift effect is observable since 2019, but the overall influences on the surface reflectance, TOA reflectance, and their derived NDVI value were very limited until 2020. The orbit drift effect was more substantial for NIR, and two SWIR bands, but less for the visible bands. Moreover, the effect was different for various land cover types, and was particularly noticeable for the cultivated, forest, grassland, and shrubland. On the other hand, the effect on TOA reflectance and its derived NDVI value will be much more severe in the future and Landsat 7 data may not be useable for certain remote sensing applications for 2021 and beyond if the orbit drift effect is not corrected. Finally, the c-factor BRDF method can reduce the effect of Landsat 7's

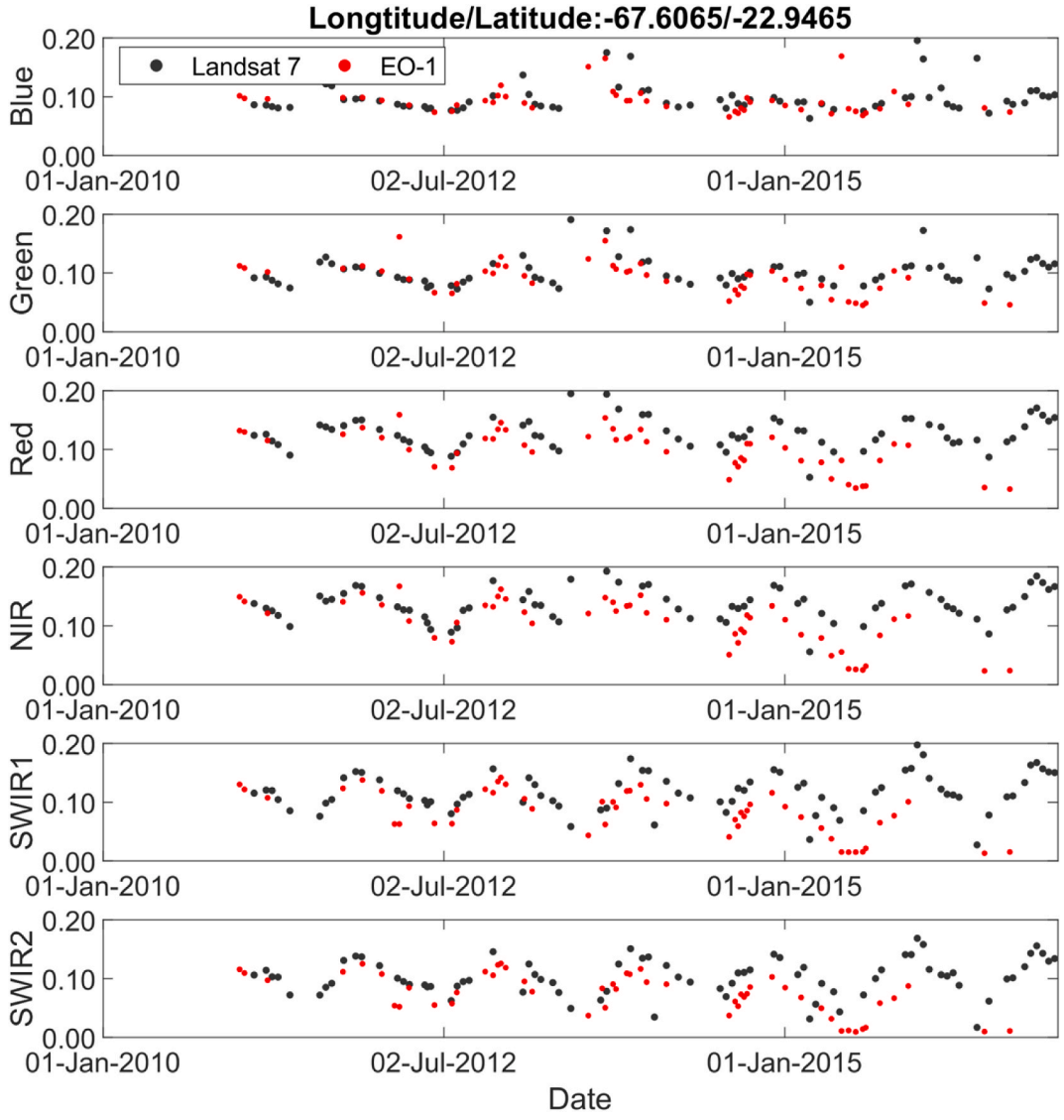

Fig. 13. Time series of Landsat 7 and EO-1 TOA reflectance between 2010 and 2016 over a forest pixel. Cloud, cloud shadow, and snow were excluded.

orbit drift that occurred in 2019 and 2020, but how it works for future Landsat 7 observations requires further study.

Declaration of competing interest

The authors declare that they have no known competing financial interests or personal relationships that could have appeared to influence the work reported in this paper.

Acknowledgments

The authors wish to thank the three anonymous reviewers for insightful comments. This study was supported by a USGS-NASA Landsat Science Team (LST) contract #140G0119C0008 to the University of Connecticut Storrs (Toward Near Real-time Monitoring and Characterization of Land Surface Change for the Conterminous US). Any use of trade, firm, or product names is for descriptive purposes only and does not imply endorsement by the U.S. Government.

References

Anderson, M.C., Allen, R.G., Morse, A., Kustas, W.P., 2012. Use of Landsat thermal imagery in monitoring evapotranspiration and managing water resources. Remote Sens. Environ. 122, 50–65. https://doi.org/10.1016/j.rse.2011.08.025.

Brown, J.F., Tollerud, H.J., Barber, C.P., Zhou, Q., Dwyer, J.L., Vogelmann, J.E., Loveland, T.R., Woodcock, C.E., Stehman, S.V., Zhu, Z., Pengra, B.W., 2020. Lessons learned implementing an operational continuous United States national land change monitoring capability: the Land Change Monitoring, Assessment, and Project (LCMAP) approach. Remote Sens. Environ. 238, 111356 https://doi.org/10.1016/j.rse.2019.111356.

Chander, G., Markham, B.L., Helder, D.L., 2009. Summary of current radiometric calibration coefficients for Landsat MSS, TM, ETM+, and EO-1 ALI sensors. Remote Sens. Environ. 113, 893–903. https://doi.org/10.1016/j.rse.2009.01.007.

Chen, Jun, Chen, Jin, Liao, A., Cao, X., Chen, L., Chen, X., He, C., Han, G., Peng, S., Lu, M., Zhang, W., Tong, X., Mills, J., 2015. Global land cover mapping at 30 m resolution: a POK-based operational approach. ISPRS J. Photogrammetry Remote Sens. 103, 7–27. https://doi.org/10.1016/j.isprsjprs.2014.09.002.

Claverie, M., Ju, J., Masek, J.G., Dungan, J.L., Vermote, E.F., Roger, J.C., Skakun, S.V., Justice, C., 2018. The harmonized Landsat and Sentinel-2 surface reflectance data set. Remote Sens. Environ. 219, 145–161. https://doi.org/10.1016/j.rse.2018.09.002.

Claverie, M., Vermote, E.F., Franch, B., Masek, J.G., 2015. Evaluation of the Landsat-5 TM and Landsat-7 ETM+ surface reflectance products. Remote Sens. Environ. 169, 390–403. https://doi.org/10.1016/j.rse.2015.08.030.

Dare, P.M., 2005. Shadow analysis in high-resolution satellite imagery of urban areas. Photogramm. Eng. Rem. Sens. 71, 169–177. https://doi.org/10.14358/PERS.71.2.169.

DeVries, B., Verbesselt, J., Kooistra, L., Herold, M., 2015. Robust monitoring of small-scale forest disturbances in a tropical montane forest using Landsat time series. Remote Sens. Environ. 161, 107–121. https://doi.org/10.1016/j.rse.2015.02.012.

Dwyer, J., Roy, D., Sauer, B., Jenkerson, C., Zhang, H., Lymburner, L., 2018. Analysis Ready data: enabling analysis of the landsat archive. Rem. Sens. 10, 1363. https://doi.org/10.3390/rs10091363.

Foga, S., Scaramuzza, P.L., Guo, S., Zhu, Z., Dilley, R.D., Beckmann, T., Schmidt, G.L., Dwyer, J.L., Joseph Hughes, M., Laue, B., 2017. Cloud detection algorithm comparison and validation for operational Landsat data products. Remote Sens. Environ. 194, 379–390. https://doi.org/10.1016/j.rse.2017.03.026.

Franks, S., Neigh, C.S.R., Campbell, P.K., Sun, G., Yao, T., Zhang, Q., Huemmrich, K.F., Middleton, E.M., Ungar, S.G., Frye, S.W., 2017. EO-1 data quality and sensor stability with changing orbital precession at the end of a 16 year mission. Rem. Sens. 9, 412. https://doi.org/10.3390/rs9050412.

Gao, F., He, T., Masek, J.G., Shuai, Y., Schaaf, C.B., Wang, Z., 2014. Angular effects and correction for medium resolution sensors to support crop monitoring. IEEE J. Sel. Top. Appl. Earth Obs. Remote Sens. 7, 4480–4489. https://doi.org/10.1109/JSTARS.2014.2343592.

Gao, F., Jin, Y., Schaaf, C.B., Strahler, A.H., 2002. Bidirectional NDVI and atmospherically resistant BRDF inversion for vegetation canopy. IEEE Trans. Geosci. Rem. Sens. 40, 1269–1278. https://doi.org/10.1109/TGRS.2002.800241.

Giles, P.T., 2001. Remote sensing and cast shadows in mountainous terrain. Photogramm. Eng. Rem. Sens. 67, 833–839.

Gorelick, N., Hancher, M., Dixon, M., Ilyushchenko, S., Thau, D., Moore, R., 2017. Google Earth engine: planetary-scale geospatial analysis for everyone. Remote Sens. Environ. 202, 18–27. https://doi.org/10.1016/j.rse.2017.06.031.

Goward, S.N., Masek, J.G., Williams, D.L., Irons, J.R., Thompson, R.J., 2001. The Landsat 7 mission: terrestrial research and applications for the 21st century. Remote Sens. Environ. 78, 3–12. https://doi.org/10.1016/S0034-4257(01)00262-0.

Gu, D., Gillespie, A., 1998. Topographic normalization of Landsat TM images of forest based on subpixel Sun-canopy-sensor geometry. Remote Sens. Environ. 64, 166–175. https://doi.org/10.1016/S0034-4257(97)00177-6.

Jacquemoud, S., Verhoef, W., Baret, F., Bacour, C., Zarco-Tejada, P.J., Asner, G.P., François, C., Ustin, S.L., 2009. PROSPECT+ SAIL models: a review of use for vegetation characterization. Remote Sens. Environ. 113, S56–S66. https://doi.org/10.1016/j.rse.2008.01.026.

Ju, J., Masek, J.G., 2016. The vegetation greenness trend in Canada and US Alaska from 1984–2012 Landsat data. Remote Sens. Environ. 176, 1–16. https://doi.org/10.1016/j.rse.2016.01.001.

Kennedy, R.E., Yang, Z., Cohen, W.B., 2010. Detecting trends in forest disturbance and recovery using yearly Landsat time series: 1. LandTrendr—temporal segmentation algorithms. Remote Sens. Environ. 114, 2897–2910. https://doi.org/10.1016/j.rse.2010.07.008.

Li, X., Strahler, A.H., 1992. Geometric-optical bidirectional reflectance modeling of the discrete crown vegetation canopy: effect of crown shape and mutual shadowing. IEEE Trans. Geosci. Rem. Sens. 30, 276–292.

Loveland, T.R., Dwyer, J.L., 2012. Landsat: building a strong future. Remote Sens. Environ. 122, 22–29. https://doi.org/10.1016/j.rse.2011.09.022.

Masek, J.G., Vermote, E.F., Saleous, N.E., Wolfe, R., Hall, F.G., Huemmrich, K.F., Gao, F., Kutler, J., Lim, T.-K., 2006. A Landsat surface reflectance dataset for North America, 1990-2000. Geosci. Rem. Sens. Lett. IEEE 3, 68–72. https://doi.org/10.1109/LGRS.2005.857030.

Masek, J.G., Wulder, M.A., Markham, B., McCorkel, J., Crawford, C.J., Storey, J., Jenstrom, D.T., 2020. Landsat 9: empowering open science and applications through continuity. Remote Sens. Environ. 248, 111968 https://doi.org/10.1016/j.rse.2020.111968.

Pflugmacher, D., Cohen, W.B., Kennedy, R.E., Yang, Z., 2014. Using Landsat-derived disturbance and recovery history and lidar to map forest biomass dynamics. Remote Sens. Environ. 151, 124–137. https://doi.org/10.1016/j.rse.2013.05.033.

Qiu, S., Zhu, Z., He, B., 2019. Fmask 4.0: improved cloud and cloud shadow detection in Landsats 4–8 and Sentinel-2 imagery. Remote Sens. Environ. https://doi.org/10.1016/j.rse.2019.05.024.

Ranson, K.J., Daughtry, C.S.T., 1987. Scene shadow effects on multispectral response. IEEE Trans. Geosci. Rem. Sens. GE-25, 502–509. https://doi.org/10.1109/TGRS.1987.289863.

Ross, J., 1981. The Radiation Regime and Architecture of Plant Stands. Dr. W. Junk.

Roujean, J., Leroy, M., Deschamps, P., 1992. A bidirectional reflectance model of the Earth's surface for the correction of remote sensing data. J. Geophys. Res. Atmos. 97, 20455–20468.

Roy, D.P., Li, Z., Zhang, H.K., Huang, H., 2020. A conterminous United States analysis of the impact of Landsat 5 orbit drift on the temporal consistency of Landsat 5 Thematic Mapper data. Remote Sens. Environ. 240, 111701 https://doi.org/10.1016/j.rse.2020.111701.

Roy, D.P., Zhang, H.K., Ju, J., Gomez-Dans, J.L., Lewis, P.E., Schaaf, C.B., Sun, Q., Li, J., Huang, H., Kovalskyy, V., 2016. A general method to normalize Landsat reflectance data to nadir BRDF adjusted reflectance. Remote Sens. Environ. 176, 255–271. https://doi.org/10.1016/j.rse.2016.01.023.

Schaaf, C.B., Gao, F., Strahler, A.H., Lucht, W., Li, X., Tsang, T., Strugnell, N.C., Zhang, X., Jin, Y., Muller, J.-P.P., Lewis, P., Barnsley, M., Hobson, P., Disney, M., Roberts, G., Dunderdale, M., Doll, C., D'Entremont, R.P., Hu, B., Liang, S., Privette, J.L., Roy, D., 2002. First operational BRDF, albedo nadir reflectance products from MODIS. Remote Sens. Environ. 83, 135–148. https://doi.org/10.1016/S0034-4257(02)00091-3.

Schott, J., Gerace, A., Woodcock, C.E., Wang, S., Zhu, Z., Wynne, R., Blinn, C., 2016. The impact of improved signal-to-noise ratios on algorithm performance: Case studies for Landsat class instruments. Remote Sens. Environ. 185, 37–45. https://doi.org/10.1016/j.rse.2016.04.015.

Shuai, Y., Masek, J.G., Gao, F., Schaaf, C., Tao, H., 2014. An approach for the long-term 30-m land surface snow-free albedo retrieval from historic Landsat surface reflectance and MODIS-based a priori anisotropy knowledge. Remote Sens. Environ. 152, 467–479. https://doi.org/10.1016/j.rse.2014.07.009.

Sims, D.A., Rahman, A.F., Vermote, E.F., Jiang, Z., 2011. Seasonal and inter-annual variation in view angle effects on MODIS vegetation indices at three forest sites. Remote Sens. Environ. 115, 3112–3120. https://doi.org/10.1016/j.rse.2011.06.018.

Sulla-Menashe, D., Woodcock, C.E., Friedl, M.A., 2018. Canadian boreal forest greening and browning trends: an analysis of biogeographic patterns and the relative roles of disturbance versus climate drivers. Environ. Res. Lett. 13, 14007.

Swinnen, E., Verbeiren, S., Deronde, B., Henry, P., 2014. Assessment of the impact of the orbital drift of SPOT-VGT1 by comparison with SPOT-VGT2 data. Int. J. Rem. Sens. 35, 2421–2439. https://doi.org/10.1080/01431161.2014.883100.

Tan, B., Masek, J.G., Wolfe, R., Gao, F., Huang, C., Vermote, E.F., Sexton, J.O., Ederer, G., 2013. Improved forest change detection with terrain illumination corrected Landsat images. Remote Sens. Environ. 136, 469–483. https://doi.org/10.1016/j.rse.2013.05.013.

Verhoef, W., 1984. Light scattering by leaf layers with application to canopy reflectance modeling: the SAIL model. Remote Sens. Environ. 16, 125–141.

Vermote, E., Justice, C., Claverie, M., Franch, B., 2016. Preliminary analysis of the performance of the Landsat 8/OLI land surface reflectance product. Remote Sens. Environ. 185, 46–56. https://doi.org/10.1016/j.rse.2016.04.008.

Vicente-Serrano, S.M., Pérez-Cabello, F., Lasanta, T., 2008. Assessment of radiometric correction techniques in analyzing vegetation variability and change using time series of Landsat images. Remote Sens. Environ. 112, 3916–3934. https://doi.org/10.1016/j.rse.2008.06.011.

Wang, Z., Schaaf, C.B., Strahler, A.H., Chopping, M.J., Román, M.O., Shuai, Y., Woodcock, C.E., Hollinger, D.Y., Fitzjarrald, D.R., 2014. Evaluation of MODIS albedo product (MCD43A) over grassland, agriculture and forest surface types during dormant and snow-covered periods. Remote Sens. Environ. 140, 60–77. https://doi.org/10.1016/j.rse.2013.08.025.

Weng, Q., Lu, D., Schubring, J., 2004. Estimation of land surface temperature–vegetation abundance relationship for urban heat island studies. Remote Sens. Environ. 89, 467–483. https://doi.org/10.1016/j.rse.2003.11.005.

Wloczyk, C., Richter, R., Borg, E., Neubert, W., 2006. Sea and lake surface temperature retrieval from Landsat thermal data in Northern Germany. Int. J. Rem. Sens. 27, 2489–2502. https://doi.org/10.1080/01431160500300206.

Woodcock, C.E., Allen, R., Anderson, M., Belward, A., Bindschadler, R., Cohen, W., Gao, F., Goward, S.N., Helder, D., Helmer, E., Nemani, R., Oreopoulos, L., Schott, J., Thenkabail, P.S., Vermote, E.F., Vogelmann, J., Wulder, M.A., Wynne, R., 2008. Free access to landsat imagery. Science (80-.) 320. https://doi.org/10.1126/science.320.5879.1011a, 1011–1011.

Wulder, M.A., Loveland, T.R., Roy, D.P., Crawford, C.J., Masek, J.G., Woodcock, C.E., Allen, R.G., Anderson, M.C., Belward, A.S., Cohen, W.B., Dwyer, J., Erb, A., Gao, F., Griffiths, P., Helder, D., Hermosilla, T., Hipple, J.D., Hostert, P., Hughes, M.J., Huntington, J., Johnson, D.M., Kennedy, R., Kilic, A., Li, Z., Lymburner, L., McCorkel, J., Pahlevan, N., Scambos, T.A., Schaaf, C., Schott, J.R., Sheng, Y., Storey, J., Vermote, E., Vogelmann, J., White, J.C., Wynne, R.H., Zhu, Z., 2019. Current status of Landsat program, science, and applications. Remote Sens. Environ. 225, 127–147. https://doi.org/10.1016/j.rse.2019.02.015.

Yang, Y., Anderson, M., Gao, F., Hain, C., Noormets, A., Sun, G., Wynne, R., Thomas, V., Sun, L., 2020. Investigating impacts of drought and disturbance on evapotranspiration over a forested landscape in North Carolina, USA using high spatiotemporal resolution remotely sensed data. Remote Sens. Environ. 238, 111018 https://doi.org/10.1016/j.rse.2018.12.017.

Zhang, H.K., Roy, D.P., 2016. Landsat 5 Thematic Mapper reflectance and NDVI 27-year time series inconsistencies due to satellite orbit change. Remote Sens. Environ. 186, 217–233. https://doi.org/10.1016/j.rse.2016.08.022.

Zhang, H.K., Roy, D.P., Kovalskyy, V., 2015. Optimal solar geometry definition for global long-term Landsat time-series bidirectional reflectance normalization. IEEE Trans. Geosci. Rem. Sens. 54, 1410–1418. https://doi.org/10.1109/TGRS.2015.2480684.

Zhang, H.K., Roy, D.P., Yan, L., Li, Z., Huang, H., Vermote, E., Skakun, S., Roger, J.-C., 2018. Characterization of Sentinel-2A and Landsat-8 top of atmosphere, surface, and nadir BRDF adjusted reflectance and NDVI differences. Remote Sens. Environ. 215, 482–494. https://doi.org/10.1016/j.rse.2018.04.031.

Zhou, L., Tian, Y., Myneni, R.B., Ciais, P., Saatchi, S., Liu, Y.Y., Piao, S., Chen, H., Vermote, E.F., Song, C., 2014. Widespread decline of Congo rainforest greenness in the past decade. Nature 509, 86–90. https://doi.org/10.1038/nature13265.

Zhu, Z., 2017. Change detection using landsat time series: a review of frequencies, preprocessing, algorithms, and applications. ISPRS J. Photogrammetry Remote Sens. 130, 370–384. https://doi.org/10.1016/j.isprsjprs.2017.06.013.

Zhu, Z., Fu, Y., Woodcock, C.E., Olofsson, P., Vogelmann, J.E., Holden, C., Wang, M., Dai, S., Yu, Y., 2016. Including land cover change in analysis of greenness trends using all available Landsat 5, 7, and 8 images: a case study from Guangzhou, China (2000–2014). Remote Sens. Environ. 185, 243–257. https://doi.org/10.1016/j.rse.2016.03.036.

Zhu, Z., Qiu, S., He, B., Deng, C., 2018. Cloud and cloud shadow detection for Landsat images : the fundamental basis for analyzing Landsat time series. Remote Sens. Time Ser. Image Process 3–24. https://doi.org/10.1201/9781315166636-10.

Zhu, Z., Wang, S., Woodcock, C.E., 2015. Improvement and expansion of the Fmask algorithm: cloud, cloud shadow, and snow detection for Landsats 4-7, 8, and Sentinel 2 images. Remote Sens. Environ. 159, 269–277. https://doi.org/10.1016/j.rse.2014.12.014.

Zhu, Z., Woodcock, C.E., 2014. Continuous change detection and classification of land cover using all available Landsat data. Remote Sens. Environ. 144, 152–171. https://doi.org/10.1016/j.rse.2014.01.011.

Zhu, Z., Woodcock, C.E., 2012. Object-based cloud and cloud shadow detection in Landsat imagery. Remote Sens. Environ. 118, 83–94. https://doi.org/10.1016/j.rse.2011.10.028.

Zhu, Z., Wulder, M.A., Roy, D.P., Woodcock, C.E., Hansen, M.C., Radeloff, V.C., Healey, S.P., Schaaf, C., Hostert, P., Strobl, P., Pekel, J.F., Lymburner, L., Pahlevan, N., Scambos, T.A., 2019. Benefits of the free and open Landsat data policy. Remote Sens. Environ. 224, 382–385. https://doi.org/10.1016/j.rse.2019.02.016.